Engineering with Computers
https://doi.org/10.1007/s00366-022-01690-x

ORIGINAL ARTICLE

# The design and application of a diffusion tensor informed finite-element model for exploration of uniaxially prestressed muscle architecture in magnetic resonance imaging

**Joseph Crutison**[1] · **Thomas Royston**[1]

Received: 1 December 2021 / Accepted: 6 June 2022


**Abstract**
The combination of finite-element models with medical imaging has been a valuable contribution to our understanding of tissue mechanics. In recent years, diffusion tensor imaging has aided in modeling axonal tracts in the brain to measure mechanical stresses related to traumatic brain injuries. Other biological systems and diagnostic techniques can benefit from this approach. Dynamic elastography is a phase contrast imaging technique, where contrast is linked to the mechanical properties (elasticity and viscosity) of the imaged tissue. Mechanical properties are obtained from solving an inverse system based on mechanical wave motion, typically under the assumption that the tissue is homogeneous, isotropic and without initial (pre) stresses or strains. Biological tissues, however, rarely have all three of these properties and the degree to which these assumptions are inaccurate can lead to poor estimates. Muscle typically violates all three major assumptions and requires more refined approaches for elastic moduli estimation. using magnetic resonance-based diffusion tensor (DT) imaging to inform the generation of subject-specific finite-element (FE) models addresses this problem by explicitly accommodating for variations in muscle architecture. This allows for a more robust analysis of prestressed wave motion while compensating for situational geometric changes induced by the loading. The presented work demonstrates a pipeline from DT imaging to FE models and the resulting comparisons with analogous MR elastography experiments. This work will help in developing anisotropic and prestressed relevant inversion algorithms, therefore, improving the accuracy of muscle elastic and viscous moduli estimates.

**Keywords** Elastography · Finite-element analysis · Diffusion tensor imaging · Acoustics · Computational Modeling · Skeletal muscle

## 1 Introduction

### 1.1 Background and motivation

Elastography is an emerging contrast method that is applied to ultrasound (US), magnetic resonance (MR) imaging and optical coherence tomography (OCT) and aims to provide a quantitative value of the mechanical properties of tissue by measuring and interpreting deformation caused by complex waves. The elasticity tensor is an important component of pathology as pathogenesis is often accompanied by strong microstructural changes within the tissue, which is evident in histological examination [1–3]. Core tenants in structural engineering provide the case that elastic moduli are products of material structure, and therefore, it should be possible to infer structural changes through measuring material property changes [3–6]. Elastography-based viscoelastic estimations of biological tissue have often assumed isotropy, homogeneity, and no (zero) loading, or prestress. In recent years, however, groups have been expanding dynamic elastography measurements to include anisotropy [7–10]. Despite this addition, the field still neglects prestress effects, which may impact the characteristics of wave propagation and lead to error. Previous analytical models have shown that wave speed is dependent on prestress in isotropic media [11]. These effects are expected to be greater in anisotropic media and may explain variation within current reported estimates,

✉ Joseph Crutison
jcruti2@uic.edu

[1] Richard and Loan Hill Department of Biomedical Engineering, University of Illinois Chicago, 851 S. Morgan St., Chicago, IL 60607, USA

Published online: 30 June 2022

especially when looking at the inaccuracies of fast shear wave estimation [7, 12]. Typically, assumptions of unloaded material were made for larger organs located in the viscera, such as the liver. However, tissues, such as muscle, or even more complex states of liver measurements, are under varying static or quasistatic loads that are non-negligible in value as compared to their elastic moduli, making it important to account for prestress in their material property estimation.

In 2007 the Radiological Society of North America (RSNA) formed a group dedicated to "improve the value and practicality of quantitative imaging biomarkers by reducing variability across devices, sites, patients and time" as described in their mission statement [13]. Key factors that determine the quality of quantitative biomarker are as follows [14]:

1. There is demonstrable validation for the precision and accuracy of a biomarker
2. There is an associated clinical endpoint
3. There is consistency with repeated measurements of the same sample
4. There is consistency between the measurements by separate groups, machines or other operation dependent conditions
5. There is satisfactory performance of the biomarker for its intended purpose

Elastography is well on its way to becoming a viable and useful biomarker, but it currently falls short when evaluating it based on these guidelines.

Specifically looking at points 3–4 above, it is necessary to understand the construction of an elastogram. As an engineering concept, there exists a system with user input of a known harmonic function that acts on a material resulting in deformation. The forward problem of this scenario asks what the deformation is given a set of material properties, while the inverse problem asks what the material properties are given a set of deformations over the body. The elastogram is an attempt to solve the latter, and aptly named the 'inversion' process. Elastography as we see in clinical practice, widely uses a form of inversion, where the phase speed of a wave is proportional to the square root of the shear modulus. This proportionality is dependent on the tissue structure being isotropic, homogeneous, and without any preloading, which is a weak assumption for almost every organ or disease process.

Due to this, the measurements obtained using these assumptions can are classified as an effective modulus and may vary based on the operating conditions and could explain the wide variability in measurements. For example, differing regions of the same muscle may have differing group fiber directions. If the actuated motion is the same direction in both measurements, the same muscle will have different wave characteristics depending on where the measurement is taken. This could alternatively be a good finding for specificity, but only in the appreciation of how anisotropy influence waves. Without that appreciation, variability will exist. It is important to move from effective measurements to more robust ones as the use of the technology expands, which is fortunately the case in anisotropic elastography [7–10, 15–17].

Structure is not the only source of variation in material properties though. Prestress is present in many biological systems as induced pressure from the cardiac cycle [18], compression from surrounding structures [19] and tension from lengthening–shortening cycles of motion. As another example, portal hypertension may cause a buildup of pressure within the liver parenchyma; finding a nominal shear modulus for one group under specific conditions (presence of non-alcoholic fatty liver disease (NAFLD), no portal hypertension) may not be the same for another group with slightly altered conditions (presence of NAFLD, with portal hypertension). Several studies already show that there are measurable and highly correlated differences with hepatic venous pressure and measured stiffness within these patients and more severe progressions of the disease [20, 21]. Without appreciation for prestress, distinct groups such as these could ruin standardization of liver stiffness due to the clear confounding factor of pressure changes, but with proper appreciation, there could be potential for high specificity screening.

As stated previously, several groups have breached the subject of anisotropy in elastography, but none have built anatomically accurate FE models to explore its effects as it relates to prestress. In non-elastography based groups that study trauma of the brain and spine, there has been an effort to combine DT imaging with FE models [24–26]; however, within these models, it is difficult to simulate harmonic wave sources at specific locations, and the resolution and sampling intervals do not meet the requirements for signal processing [27].

Combining anisotropy and prestress further complicates the problem as the way stress distributes is necessary to understand and prevent it from becoming a confounding factor [22]. Complex, dynamic tissues, such as muscle non-uniformly disperses stress throughout, leading to variation in the prestressed wave patterns based on location of the measurement [23]. Hence, two major questions arise: to what level does prestress effect shear wave propagation in different tissue architectures and how should one remove, or account for, the effect.

### 1.2 Objectives

This research aims to begin answering these questions through the design of an algorithm that converts diffusion

tensor (DT) imaging data into finite-element (FE) models that satisfy criteria for simulations of elastography. Extending on the methods of DT–FE algorithms used in other fields, but satisfying wave processing requirements, will allow for more in-depth analysis of wave propagation in complex tissues.

## 2 Methods

Figure 1 shows the overall steps taken from image acquisition to simulation. Each step will be broken down for further explanation.

### 2.1 Image segmentation

The model was first built using DT images obtained from the open-source database created by Bolsterlee et al. [28] MR magnitude images of the human lower leg from this database were taken on a 3 T scanner using the following parameters: TR/TE of 1842/8 ms, with a $288 \times 215$ data matrix for a voxel size of $0.1875 \times 0.1875$x5mm. DT images had a TR/TE of 8522/63 ms, voxel size of $1.875 \times 1.875 \times 5$ mm, 16 directions with 2 averages and a $b$ value of 500 s/mm$^2$. After the algorithm was designed, it was later tested on in-house scans, where additional MR wave images could be captured to verify the process. In-house scans were done on fresh chicken breast obtained from a local butcher shop (see verification of finite-element simulation for imaging parameters). All MR magnitude images were initially converted to 3D models using a commercially available software, ITK–SNAP [29], which output stereolithography (STL) files. The choice in using this method allows for any 'MRI-to-3D model' tool to be used as the initial step in segmenting anatomy. STL files are built upon trigonal meshing, which convolutes the original slice planes, as any mesh face can span multiple slices. If the resolution of the scan slice thickness is not fine enough, the 3D model will be blocky, as shown in Figs. 2a and 3a. This also will create an issue, where there is no logical ordering to the vertices, making it difficult to process any further.

Slices are first reconstructed through a filtering technique aimed at identifying 'Mach edges' [30, 31], where pseudocode of the algorithm is shown in Appendix A.1. A 'Mach edge' is defined as an edge between two contrasting values in a gradient (Fig. 2a, b). Assuming that the in-plane vertices are closer than slice planes, the mesh vertices transitioning between slice planes create the gradient, while edges of the blocky slice create the 'Mach edge'.

First, the Euclidean distance of each vertex from the centroid of the model is calculated using Eq. 1, where $D$ is a vector of each vertex's distance, $A$ is the original $n \times 3$ point matrix, and $C$ is the $1 \times 3$ centroid coordinate. Reordering the nodes, based on their distance, $D$ and taking the square of third derivative, or geometric torsion, of this newly ordered data set will then produce spikes at regions, where the slice plane jumps to the next (Fig. 2c). Simply filtering out all vertices lower than 1% of the max peak will get rid of most 'gradient' vertices. The vertices are filtered a second time by keeping only the slices that contain vertex counts within 1 standard

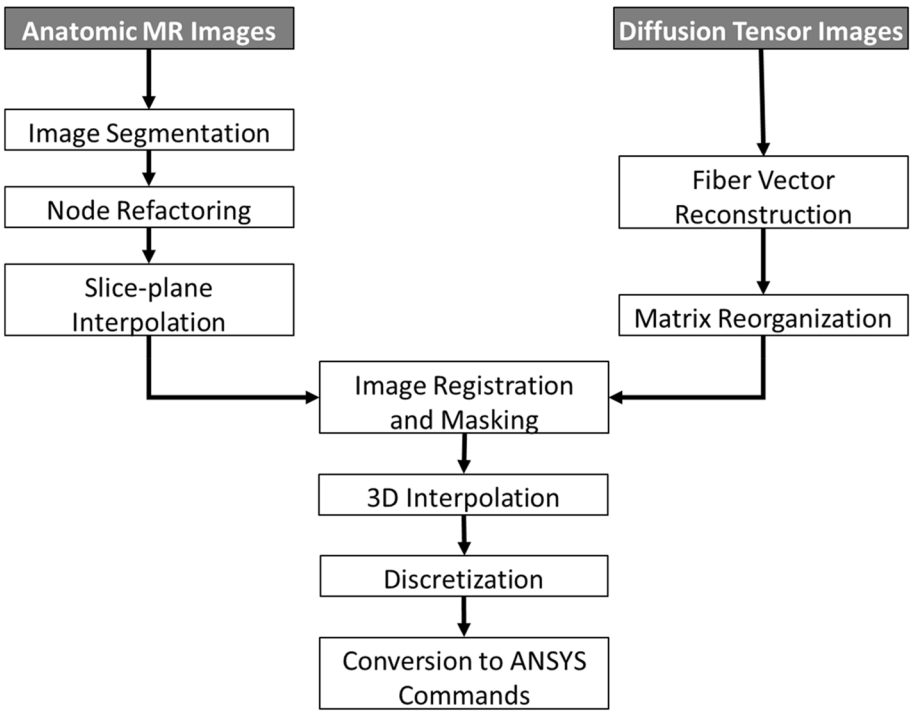


**Fig. 1** Pipeline from Image to 3D model. Flow diagram showing the major processes taken to convert a basic DT scan session into a finite-element model in ANSYS. MR magnitude images are segmented in an image segmentation software, imported into MATLAB, where nodes are refactored and interpolated for masking. DT information is processed using DSI Studio and then imported into MATLAB for masking. After registering the DT images and MR magnitude images, the fiber model is then masked and interpolated to the desired resolution and discretized for finite-element simulation

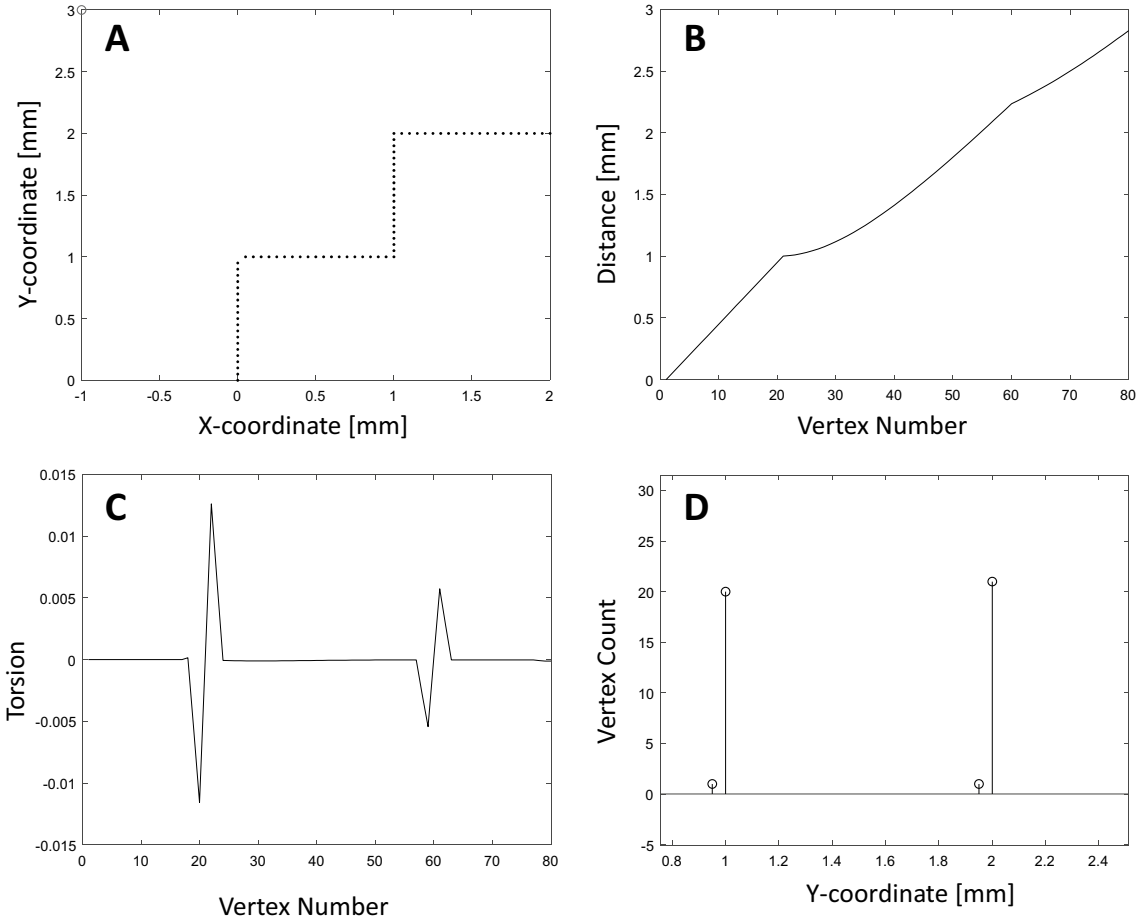


**Fig. 2** Representation of Mach Edge Decomposition. **A** Sampled vertices from two slices at $y=1$ and $y=2$. Vertices fill in the space between slices creating a blocky model. The red point at $(-1, 3)$ represents an arbitrary centroid used to calculate the distance between it and each vertex. **B** Plotted distance between the centroid and each vertex with slight peaks at the mach edge, representing the beginning of a slice. **C** Third derivative of the distances plotted against each vertex visualizes, where the slices begin (at either the peak or valley). Vertex 20 and 22 represent a band at which the first mach edge exists, the corresponding y coordinates for each are 0.095 and 1, respectively. **D** All points in the original model are counted that lie at potential mach edges, where it becomes clear that $y=1$ and $y=2$ are the slice planes

deviation from the mean count of vertices within each unique potential slice plane created from the previously filtered set (Fig. 3b). This is possible due to the number of nodes within each actual slice being substantially greater than any erroneous values elsewhere (Fig. 2d). Finally, to obtain the maximum density of nodes per slice, the original trigonal mesh faces are projected onto the doubly filtered slices (Fig. 3c):

$$D = \sqrt{(A-C)^2 \begin{Bmatrix} 1 \\ 1 \\ 1 \end{Bmatrix}}. \tag{1}$$

## 2.2 Node refactoring

The end goal is to create a discretized model with regular meshing that corresponds to the acquired DT images. Regular meshing requires two properties from the data set: the data has equally spaced vertices, and the corresponding faces are equal (i.e., all quads or all tris) [32]. We go further to include voxelwise meshing to get the closest correlation without excessive interpolation of the data. Therefore, complex approximations of non-convex hulls are not applicable. Parametric, linear, or polynomial approximations can be used for each slice shape. However, this requires logical ordering. Ordering of non-convex shapes can be difficult, so a recursive approach was applied as shown in the flow diagram, Fig. 4, and outlined in pseudocode in Appendix A.2. For each slice, a minimum of two points are found based off another chosen

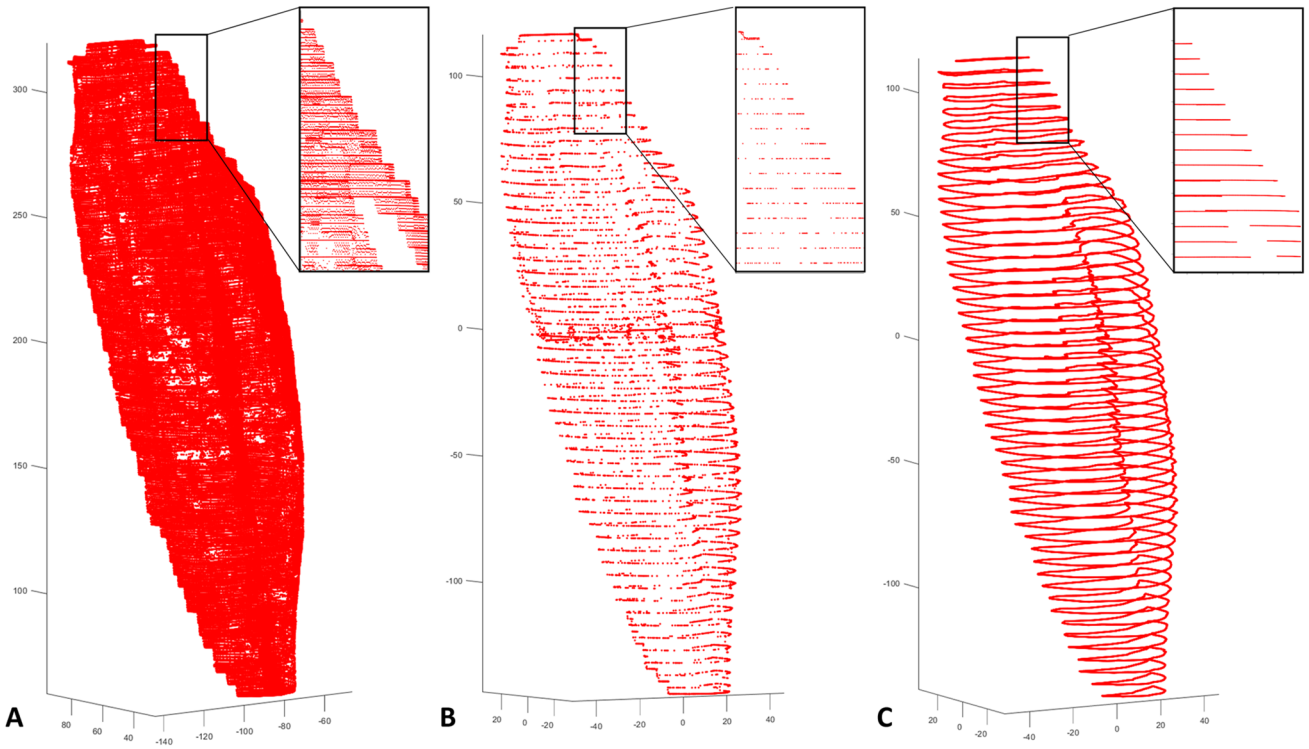


**Fig. 3** Back calculating slices from a segmentation of an in vivo scan of a human lower limb. **A** Original point cloud of the segmented soleus muscle created by ITK-Snap using a data set published by Bolsterlee et al. This shows rough transitions between slices, where nodes are not exclusively within slice planes. **B** Slice planes are filtered out using a third-order derivative signal processing filtration, to clear out remaining noise, only $z$ values with corresponding vertex count within one standard deviation from the mean $z$ value vertex count are kept. **C** Maximization of vertices is achieved by taking the filtered $z$ values and projecting all vertices from the original point cloud to the new $z$'s, setting up the best initial state for node refactoring

or random starting point by closest proximity. This gives the minimum number of points needed to create a shape; if this fails, the slice is considered a line or a point and is disregarded. A data matrix is created with these three points, and the last point is used to find the next nearest point, which is then added to the matrix. This continues until the last point to be found is the same as the first point. Any points that are not within the constructed data matrix are stored in an 'odd' matrix and sent through the same ordering process. This continues until every point has been ordered into sets. This leaves several 'odd' matrices that correspond to segments of the boundary and one 'shape' matrix roughly defines slice as a convex hull (Fig. 5b). The point of concavity will mark the end of a segment. Each segment is then connected by another recursive process. The end point of the 'shape' matrix is used to find the closest point within one of the 'odd' sets. The selected 'odd' set is then reordered based off the nearest point and the reordered nodes are connected to the starting shape, while any missed nodes are added back into the collection of 'odd' sets (Fig. 5c). This process then repeats until every set is connected. Due to the recursive nature, this process may repeat several times and break previously created segments, until a combination of points is reached such that every node has an optimal neighbor (Fig. 5d).

To decrease computational time, the number of nodes in each slice can be forced using Chebyshev spacing, which postulates a more optimal data set for approximation techniques [33]. This is outlined in pseudocode in Appendix A.3. Equations (2) and (3) give the $k$th node in Chebyshev space (written as $c$) on the interval $[a, b]$, where $k$ is every positive integer from 1 to the desired number of nodes, n:

$$c_k = (b - (b - a)/2) + \cos\left(\theta_k\right) * (b - a)/2, \tag{2}$$

$$\theta_k = \frac{k - 1}{n - 1}\pi. \tag{3}$$

Coordinates of the above optimized nodes are found using a Lagrange approximation shown in Eqs. (4, 5). The original data set is first parameterized, where $t$ is the original number of nodes, $Y$ corresponds to the in-plane slice coordinates of the original node, $Y'$ is the optimized coordinates, and an $x$ with a subscript represents the current $i^{th}$ and $j^{th}$ original node:

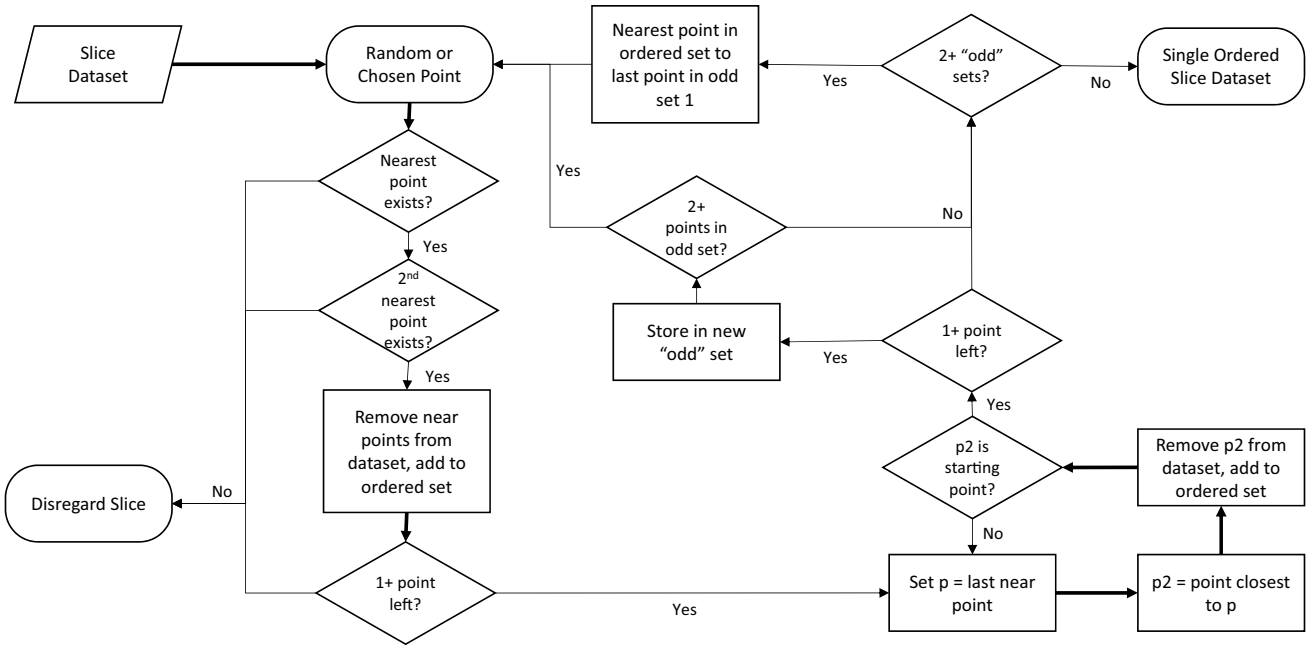


**Fig. 4** Flow diagram of ordered points algorithm. Each slice is input into the algorithm, where a vertex is chosen corresponding to the lowest y coordinate and middle x coordinate in the default 2D orientation. From this vertex, two nearest vertices are found to guarantee the slice can fit a shape. If two other vertices are not found within the entire slice, then it is rejected. From there, a recursive process finds all nearest vertices from the last active vertex until the shape is connected back to the initial vertex. All non-connected vertices are stored in a separate segment data set and repeat the process, with the exception of rejecting the entire slice. Once all vertices are connected via the segment they are in, the segments are connected to each other through a nearest neighbors' algorithm and their vertices are reordered, where the starting point is now the connecting vertex between segments. This process repeats until every segment is connected, producing a shape with ordered vertices

$$Y'(c) = \sum_{i=0}^{t} Y_i l_i(c), \tag{4}$$

$$l_i(c) = \prod_{j,j\neq i}^{t} \frac{c - x_j}{x_i - x_j}. \tag{5}$$

## 2.3 Diffusion tensor image processing

DSI studio was used to reconstruct fibers using a deterministic algorithm [34] and imported into MATLAB for further processing. Imported files had at least two associated data sets corresponding to a 3 by 1 vector containing the DT data matrix size, and a 1 by 3*$n$ array that specifies the decomposed directions in the $x$, $y$ and $z$ dimensions, where each vector's $x$-coordinate are the $1+3(n-1)$th data point, $y$ is the $2+3(n+1)$th data point, and $z$ is the $3+3(n-1)$th data point ($n$ being the vector node); all of which is outlined in more detail in the DSI studio manual [34]. Muscle has relatively strong anisotropy, so the main direction from the data set was assumed to be the direction of the fiber. Since the directional data set is based on a volumetric image of a size given by the dimensional vector, this subroutine simply reshapes the directional data set into a $n$ by 6 array using the dimensional vector, where n is the number of data points and the columns correspond to the coordinates of the fiber vector's origin ($x$, $y$, $z$) and the normalized direction ($u$, $v$, $w$). In this way, the first three columns fit a standard finite-element point matrix.

## 2.4 Image registration

A custom interface was developed to co-register the DT and segmented data sets. Being that the segmented data set is a derivative of the magnitude image data set, an affine linear transformation is all that is needed to register the two sets. Both the magnitude image and DT sets are multiplied by their pixel size to obtain their physical sizes, which itself registers DT and the magnitude images. The segmented data set can then be registered to the magnitude image set, which indirectly aligns it with the DT image. This step is necessary due to image segmentation software outputting their own coordinate systems for the vertices, which may or may not be stretched or rotated compared to the actual MR system.

Transformation was done using Eqs. (6–8). In affine image registration problems, one coordinate system can be transformed into another by stretching and rotating the elementary

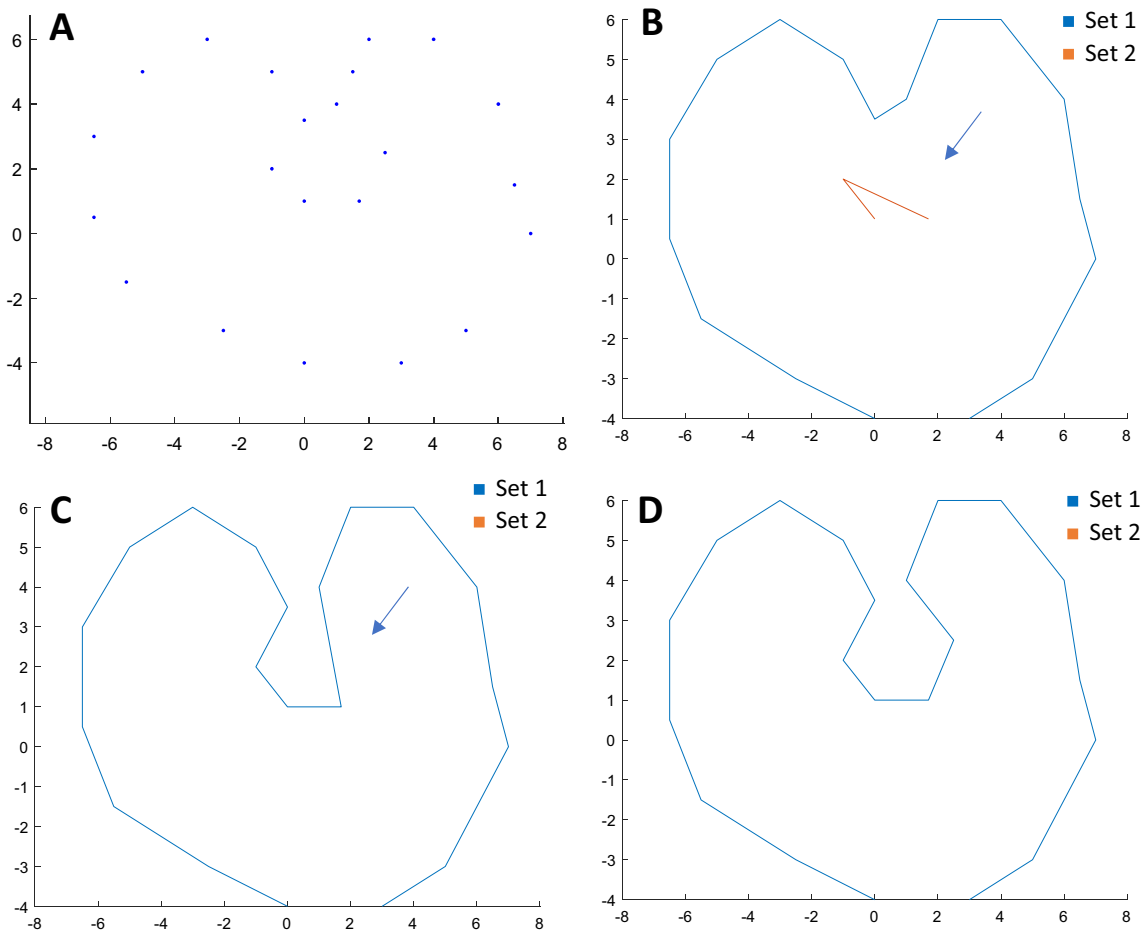


**Fig. 5** Ordering points in a concave shape. **A** Starting point cloud, where all points are assumed to create a shape with no intersecting lines. **B** After one round of the node ordering algorithm, three segments are created: one main segment and two smaller segments. The smaller segments are created and ordered by undergoing sub-rounds of the ordering process until all points are assigned a segment and ordered within its respective segment. In this example, one off set consisting of 3 points was created, followed by another off set consisting of a single point (indicated by an arrow). **C** After a second round, segments 1 and 2 are connected based on the two vertices closest to each other. The new set is reordered starting from these two vertices. The third segment remains an off set. **D** Final round connects the third segment to the larger one and all points are reordered, giving the final shape of the slice

vectors that make up the basis, and by translating the origin. Equation (6) shows $p^{'}$ as the registered point that undergoes a transformation $T$ and translation $t$. To simplify the solution, $T$ and $t$ can be combined into a matrix by concatenating columnwise and adding a row of zeros under the rotational part, and 1 to the translational part. In such a way, $T$ and $t$ can be solved simultaneously by solving a system of equations, where $p$ and $p^{'}$ are concatenated forms as shown in Eq. (8). In order for this method to work, $n+1$ equations must be used, since $T$ is an n-by-n matrix and $t$ is an n by 1 matrix, where n is the number of degrees of freedom. For example, in a 3D system, there are 12 unknowns ($3\times3$ from $T$ and $3\times1$ from $t$) and each equation has 3 knowns ($p_x$, $p_y$ and $p_z$), so 4 points will be needed to have 12 total equations. At least n points must be linearly independent to create an orthogonal basis in the transformation matrix. This means for the algorithm; each point must be manually selected from at least two different slices in a 3D data set. Figure 6 shows the selection process for a sample soleus. To ensure precision, the middle slice and one end slice in both image sets were selected and the contours were compared. Once the corresponding slices were found, landmark points are selected and used for the affine transformation:

$$p^{'} = Tp + t, Q = \begin{bmatrix} T & t \\ 0 & 1 \end{bmatrix}, \ \mathrm{p}^{'} = \mathrm{Qp}, \tag{6}$$

$$p, p^{'} = \begin{pmatrix} x \\ y \\ z \end{pmatrix}, \tag{7}$$

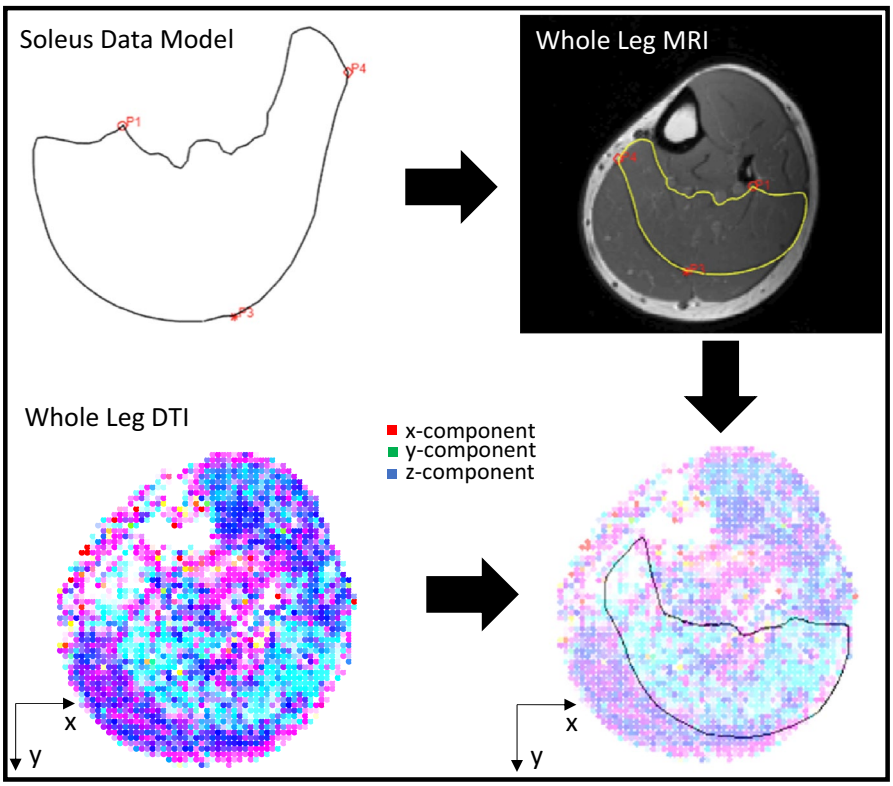


**Fig. 6** Point selection for co-registration. Top left: segmented data model of a human soleus cross section with three of the four registration points shown in red. Top right: T1-weighted image of the corresponding lower leg with superimposed data model stretched, rotated, and mirrored to align registration points. Lower left: DT fiber map of the lower leg, where colors are mixed in an RGB color scheme depending on the overall contribution to the fiber direction. Lower right: superimposed co-registered data model onto the DT fiber map, outlining the diffusion vectors belonging to the soleus. Custom Affine image registration allows for the segmented data model to be registered to the magnitude image. Superimposing this onto the DT image allows for masking based on anatomy

$$\begin{pmatrix} p'_x \\ p'_y \\ p'_z \\ 1 \end{pmatrix} = \begin{bmatrix} T_{11} & T_{12} & T_{13} & t_x \\ T_{21} & T_{22} & T_{23} & t_y \\ T_{31} & T_{32} & T_{33} & t_z \\ 0 & 0 & 0 & 1 \end{bmatrix} \begin{pmatrix} p_x \\ p_y \\ p_z \\ 1 \end{pmatrix}. \tag{8}$$

## 2.5 Shape interpolation

The correct resolution in the $z$ direction is obtained by interpolating the shape from one slice to another. The parametric interpolation technique used during the optimization process can be reused here in a modified manner. In the previous use, each slice was forced to have an equal number of nodes while also having each slice ordered in the same way from the ordering algorithm. This creates a system, where every slice has corresponding counterpart vertices amongst all slices, and therefore, counterparts can be set as data points on a curve from the minimum slice to the maximum. Interpolation of each curve based on a predefined resolution for $z$, results in interpolated slices. An example from the soleus is given in Fig. 7, interpolating two primary slices to six, where the lower is a circle and the upper is a square.

## 2.6 Fiber masking and interpolation

If the region of interest is smaller than the full specimen, the registered segmented data can be used as a mask using an efficient implementation of the winding numbers in polygon point algorithm as described by Hormann and Agathos in [35]; which samples points from one data set to determine if they are within another's boundary and outputs a logical array that meets the condition. The origins of the fiber directions in the DT data set are input as the query set and the segmented model is input as the boundary set. The output is then a voxelwise data set of only the DT data within the desired boundary. After masking, both the fiber origin coordinates and direction vectors are saved as a new $n \times 6$ matrix.

Due to the regularity of the data points, trilinear interpolation techniques are all that is needed to create artificial vectors at alternate resolutions. Here, the directional components, u, v, and w, of the fiber vector are considered separately in the system and what will be interpolated as such. Equations (4 and 5) are used in this process, where one dimension is interpolated at a time. Here, $Y'$ is now a matrix of the desired coordinates, $c$, for the respective dimension, $x$ is the original respective dimension's coordinates, and $Y$ is the original matrix. The second and third round consists of $c$ being the desired coordinates of their respective dimension, but $Y$ is now the previous round's output, $Y'$.

## 2.7 Model discretization

Ansys® Academic Research Mechanical, Release 19 was used as the targeted finite-element analyzing software.

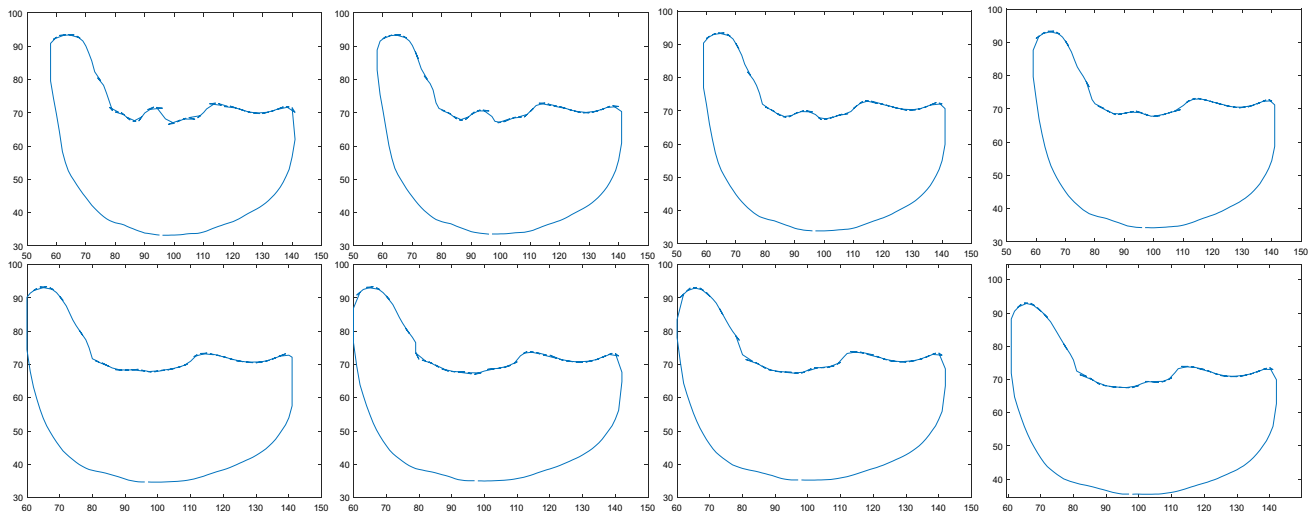

**Fig. 7** Shape interpolation. Example of interpolating two slices of the soleus in eight steps. First, Chebyshev approximation is applied to the circle and square slices to ensure corresponding vertices. Then, each vertex pair is interpolated to include seven inner slices

As defined by the accompanied documentation element index, anisotropy can be implicitly applied to hexahedral SOLID185/186 or tetrahedral SOLID187/285 elements by setting the axes of anisotropy parallel to one of the directions of the local coordinate system (Fig. 8). Local coordinate systems can be rotated relative to the global coordinate system, allowing for each element to have a unique axis of anisotropy for transversely isotropic materials. To capitalize on this and preserve the base model's fiber directionality, as well as fine control during simulation setup and post processing, voxelwise discretization procedures were opted for over standard solid meshing algorithms. The procedure is an adaptation of the marching cubes algorithm by Lorensen and Cline [36], where an iterative process moves through all voxels over the data set and marks any nodes that are at the 8 corners of the voxel. The adapted portion is to include solid cubes and tetrahedrons in the look-up table, rather than output

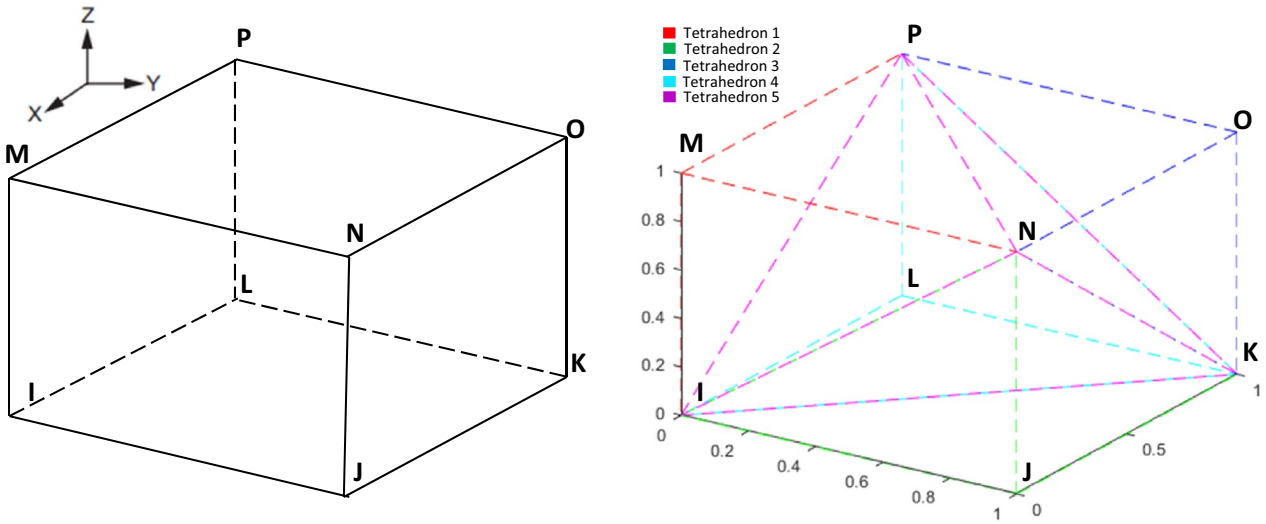


**Fig. 8** Marching cubes algorithm implementation. (Left) ANSYS node classification of hexahedral elements and orientation. (Right) Modified marching cubes includes tetrahedral elements based on node combinations. Currently showing 5 tetrahedral combinations that fit within a single hex element. By running a voxelwise meshing, the regular spacing of DT fiber coordinates can have a 1:1 fiber to element setup. For tetrahedral elements, any fiber that would have fit in the hex element is duplicated to fit in each of the tetrahedral elements

a mesh. Due to the interpolation of the earlier model, all nodes will lie at a corner. This simplifies the algorithm to handle every combination of nodes within a voxel based on a predefined set of orientations. The voxel is then labeled as 'In', 'Out', or 'Border', where 'Out' voxels are disregarded as there are no matched nodes, 'In' voxels have all their corners matched to nodes within the model, and 'Border' voxels have partial matches that can either be disregarded, or broken down into a combination of tetrahedrons that connect nodes in the model, as shown in Fig. 8.

## 2.8 Mesh refinement

Post processing of harmonic waves in elastography require that there are at least 4–8 datapoints per wavelength [27]. This requirement, along with the increased boundary errors from a voxelwise mesh mean that the model has a restricted resolution, typically weighted more towards the wave data than the geometric boundary. To avoid having needlessly fine resolutions over the entire model (and increasing computational time), the mesh is refined only at the region of interest near the wave source, while the rest of the model is set to a resolution restricted by the geometry. The two resolutions are connected using transition elements as outlined in Fig. 9a, b. This gives the advantage of having lower computational times while maintaining the necessary thresholds to reach convergence in nonlinear analyses. This style of mesh refinement is based on levels, where each $n$th level of refinement results in a reduction of $2^n$ in size of each dimension, or $2^{3n}$ more elements.

## 2.9 Verification of finite-element simulations

Verification of the model was done using experimental data collected in house. Experiments consisted of two testing pre-strains, 0% and 6% total strain on the sample, each of which was evaluated with DT imaging for fiber information and MR elastography scans for wave response. Samples consisted of store-bought fresh (not frozen) chicken breast and scans were performed on an Agilent 9.4 T 30 cm horizontal bore preclinical scanner. DT imaging values for TR/TE were 3200/10 ms with a $b$ value of 900 and 12 sampling directions with 3 averages. Sagittal scans were taken with a pixel size of $0.75 \times 0.75$ mm and data matrix of $128 \times 128$ and 40, 1.5 mm thick vertical slices.

Wave motion was applied at a frequency of 600 Hz and captured using a Sample Interval Modulation (SLIM) [37] MR elastography sequence with TR/TE values of 1600/16 ms for 30 axial slices with an isotropic voxel size of $0.75 \times 0.75 \times 0.75$ mm and data matrix size of $64 \times 64$. Eight (8) time steps with 180° offsets were taken for better unwrapping. A motion encoding gradient cycle count of 10 with a power of 250mT/m were used. Both static pre-stress and strain, overlayed with small amplitude harmonic actuation were achieved using a custom-built experimental setup that fixes one end of the sample and adds an adjustable static tension to the other end while simultaneously actuating the sample in the middle with a harmonic input. This actuation was driven by a piezo-ceramic stack (P842.10, PI USA LP) oscillating at approximately 10 µm, where motion is then transferred to a ring concentrically binding the roughly cylindrical-shaped sample with motion polarized in the axial direction, as shown in Fig. 10b.

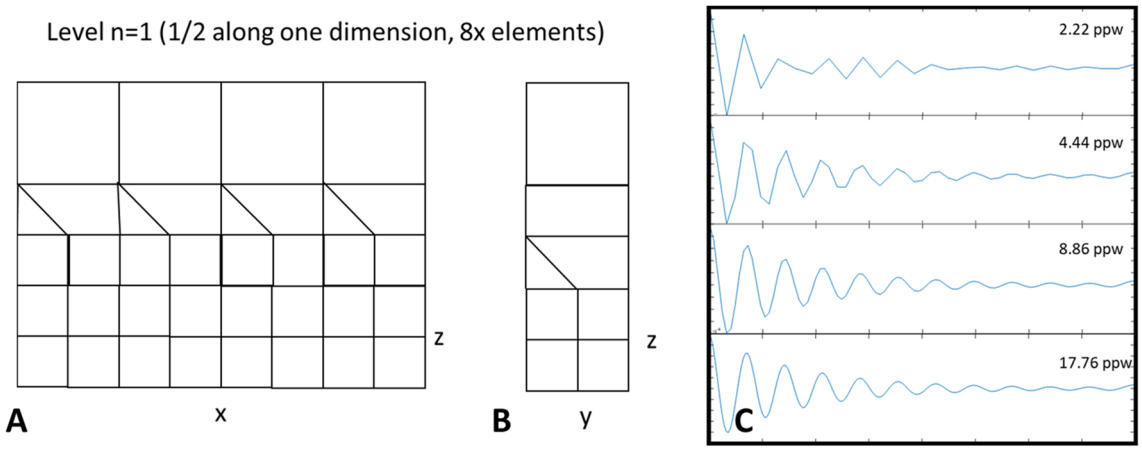


**Fig. 9** Transition elements in a voxelwise discretized model. **A** Approach to mesh refinement starting first with dividing the $z$ dimension in half and placing a node at half the $x$ dimension, allowing for hex and tetrahedral elements to still be used and keep regularity as the mesh subdivides. **B** One level below the $x$ and $z$ subdivision, $y$ is subdivided, so that all levels downstream of the subdivision now have $8\times$ the elements as the original. The process is reversed at the end of the high-resolution region. **C** Visual representation of an attenuated wave with regular sampling. At 2.2 pixels per wavelength, the wave is poorly estimated. At 8.8 pixels per wavelength, the wave is well defined, and any higher resolution has diminishing returns

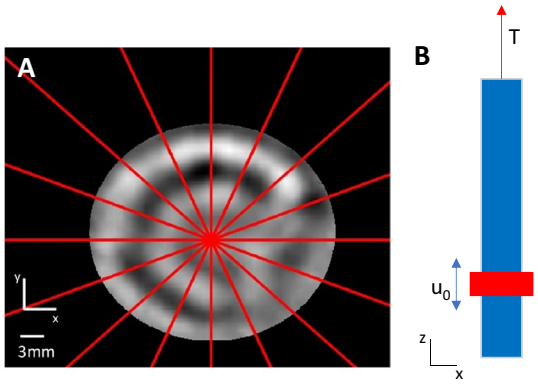


**Fig. 10** Experimental Setup and Wave Sampling. **A** Example of a masked cross-sectional wave image produced by MR elastography. Red dotted lines indicate 16 sampled waves. **B** Diagram of setup. Blue represents the cylindrical-shaped sample (chicken breast), while red represents the harmonically actuated ring that gripped the sample approximately 1/3 of the way up. Actuation location is based on a balance of torque on the piezo, and distance from the fixed (bottom) end. Axial slice images were obtained at the axial center of the ring for the strongest wave source. Tension T is applied at one end, while the other end remained fixed

Experimental wave images were analyzed to estimate the initial material properties for the sample. Wave analysis consisted of sampling the mean of 20 cross-sectional axial slices of the volumetric wave image produced by the wave source, which was 15 mm. Vibrating the sample on its outer cylindrical boundary using a ring with axially polarized motion creates a radially convergent wavefront as described by Guidetti and Royston [17], and so axial motion was measured along 128 radial line profiles, from the outer cylindrical boundary (actuator location) to the central point of convergence, as shown in Fig. 10a. Out of the 128 samples, a smaller section of 32 wave profiles that showed consistent quality in all experiments was used for the analysis. Each wave profile was fit to the wave equation, Eq. (9) to obtain the complex wave number, $K$, using a Bessel fit method which is described in detail by Yasar et al. [38] and shown in Eq. (10). Where $u_0$ is the initial amplitude, $i$ is $\sqrt{-1}$, u is the responding displacement, $x$ is the distance along the traveling wave, $t$ is time, $J_0$ is the Bessel function of the first kind, zeroth order, and $\omega$ is angular frequency. Equation (10) was fit using a least squares method, where the phase shift, wave number, and amplitude are free variables that can change with each wave profile. It is expected that the wave number, $K$, will remain relatively consistent, while the phase shifts depending on confounding factors. Doing so, the mean $K$ of all sampled wave profiles was taken as the estimated value for that experiment. The experimental MR elastography estimates were then used to determine all other material property values used in all FE simulations:

$$u = u_0 e^{i([k_{\text{real}}+ik_{\text{imag}}]x-\omega t)}, \tag{9}$$

$$u_z(x,t) = u_0 \frac{J_0(Kx)}{J_0(Kr)} e^{i\omega t}. \tag{10}$$

If fibers are oriented parallel to the axis of the cylindrical sample, both simulation and experiment are inducing "fast" (not "slow") shear waves in transversely isotropic materials, since the motion polarization is also along the cylinder axis and thus, not perpendicular to the axis of isotropy. The uniaxial static pre-stress is also parallel to the axis of isotropy in this case. Based on this, Eq. (12) describes fast shear wave speed by relating it to the density of the material, $\rho$ (assumed 1000 mg/ml for soft tissue), and the perpendicular shear modulus, $\mu_\perp$. Wave speed is estimated from $K$ using Eq. (11). The fast wave speed is a phase speed, and hence the connection to $K$ as an evaluative number. All other material properties are then found using Eqs. (13–16), which assume near incompressibility and transverse isotropy. The shear and tensile anisotropic ratio, $\varphi$ and $\zeta$ were assigned values of 0.668 and 1.37, respectively, as estimated by Guertler et al. [10] for the transversely isotropic chicken breast:

$$c_f = \frac{2\pi f}{K}, \tag{11}$$

$$c_f^2 = \frac{\mu_\perp}{\rho}(1+\phi), \tag{12}$$

$$\mu_{||} = \mu_\perp(1+\phi), \tag{13}$$

$$\delta = G''/G', \tag{14}$$

$$E_\perp = \mu_\perp(4\zeta+3), \tag{15}$$

$$E_{||} = E_\perp(\zeta+1). \tag{16}$$

The FE model mimicked the experimental MR elastography study, where the corresponding end of the model that was clamped is held fixed, while the opposing end was set with a given displacement equal to the length change obtained in the experiments. Harmonic displacements with axial polarization equaling 10 μm amplitude at 600 Hz were applied to nodes on the outer cylindrical boundary at the same location as the actuating ring in the experimental setup. Nodes at the fixed and displaced ends were allowed to rotate freely, move axially at the desired strain level and were fixed for translational motion perpendicular to the axis of tension.

First, a nonlinear static analysis was performed on the model, with ten sub steps per strain to ensure convergence, until the desired strain levels were reached. The solution was

then linearized and saved for harmonic analysis. Within the harmonic analysis, the linearized solution was loaded as a prior state so that the stiffness matrix reflected the changed material and the harmonic motion applied as an additional perturbation (solution step) in Ansys.

Due to assumption of no prestress and isotropy in using a Bessel function to solve the wave equation, 'pre' simulations were ran and compared to the experimental wave images and material properties adjusted iteratively to define the material properties for the final FE simulations. Comparison consisted of first analyzing the MR elastography, running a simulation, and then qualitatively matching wavelengths of the MR elastography to the generated FE samples and adjusting material values as needed until there was a satisfactory match both by qualitative assessment and the estimated K.

The initial material properties at 600 Hz with 0% prestrain are given in Table 1.

### 2.10 Data analysis

Wave profiles of the FE simulations were obtained as explained for the MR elastography experiments. Each wave profile was fitted using a least squares method to the closed form equation of an axially polarized wave propagating transversely in a cylinder, given by Eq. (10). The MR elastography experimental estimates were used as reference and each simulation estimation evaluated against it with a relative error.

## 3 Results

Figure 11a–-c shows the stress distributions along the entire sample and at the evaluated axial cross sections. It is important to note that sharp variations in stress manifest in the wave image as deviations from the concentric wave pattern. Tractography of the sample at 0% total strain is shown in Fig. 11a. The color scheme indicates the fiber track's primary direction: magenta corresponding to the positive x direction, green to the z direction, and blue to the *y* direction. It is important to note that the fibers are not uniform across the whole sample but are relatively uniform at a 57-degree tilt from the main axis in the actuated region.

Figure 12 shows the wave analysis done on the MR elastography acquisition (subfigures a–f) and DT informed FE (subfigures g–l), respectively, where the first and third rows correspond to 0% total strain, and second and fourth rows correspond to 6% total strain. The second and third columns show the real and imaginary fits, respectively (shown as a red line), over the sampled displacements along each wave

**Table 1** Estimated initial material properties of chicken breast

| | $\varphi$ | $\zeta$ | $\mu_{\|\|}$ | $\mu_{\perp}$ | $E_{\|\|}$ | $E_{\perp}$ | Damping |
|---|---|---|---|---|---|---|---|
| Transversely isotropic (DT informed) | 0.668 | 1.37 | 14,178 | 8500 | 72,080 | 30,414 | 0.635 |

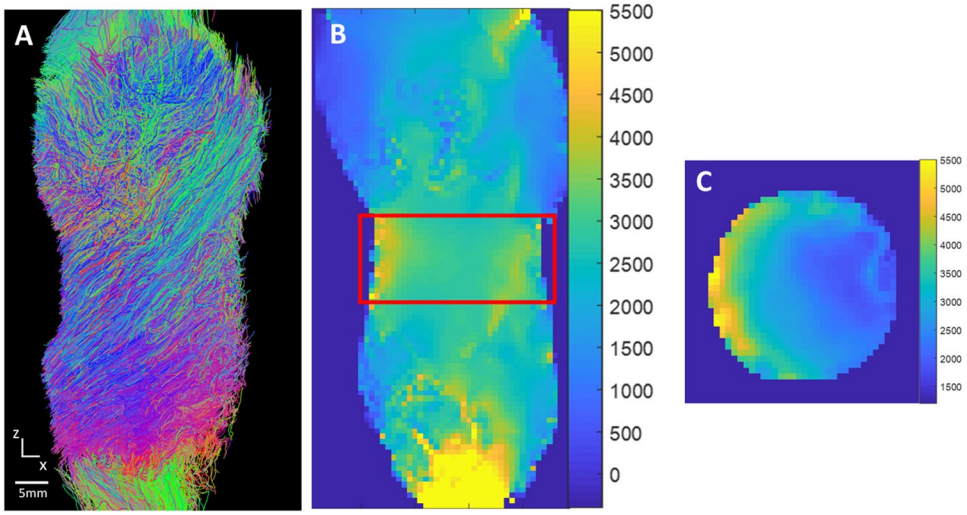


**Fig. 11** Stress analysis of finite-element solutions at 6% Total Strain. **A** Tractography of the chicken breast sample. Color scheme indicates the fiber track's primary direction: magenta corresponding to the positive x direction, green to the z direction, and blue to the y direction. Mean fiber angle from the z direction is 57 degrees within the actuated region. **B**, **C** Axial stress estimates of the DT informed FE simulations have a complex distribution of stress and highlight how anisotropic muscle affects this, even when material properties are uniform. All stresses shown in the color scale are in Pascals. **B** Sagittal cross section of the muscle sample, while (**C**) shows axial cross sections at the same location as the analyzed wave images (outlined in red on **B**). Sharp variations in stress regionally alter the wave patterns

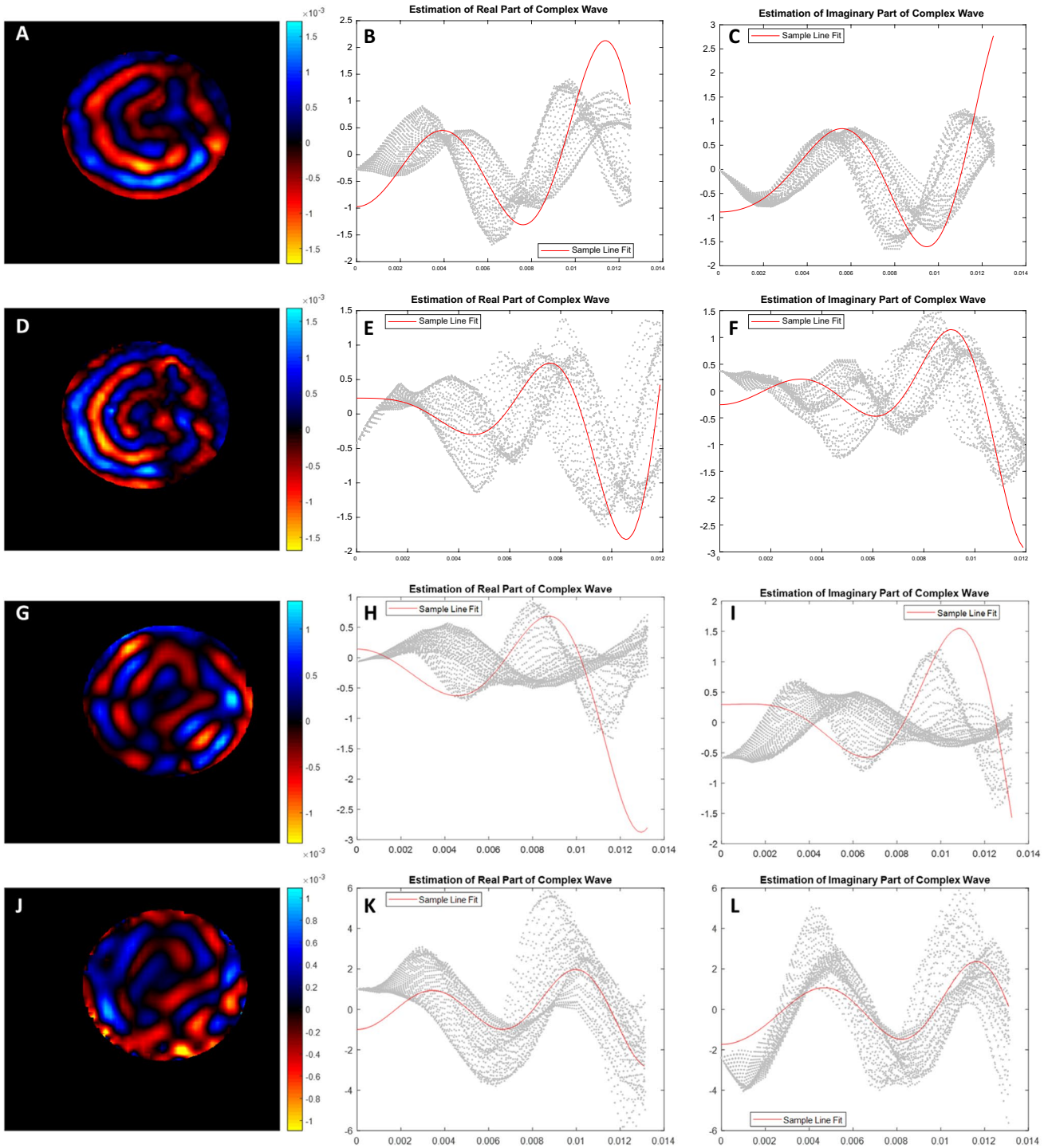


**Fig. 12** Wave analysis of MR wave image (**A**–**F**) and FE simulations (**G**–**L**). (**A**–**C**, **G**–**I**) Visualization at 0% total strain and (**D**–**F**, **J**–**L**) visualization at 6% total strain. **A**, **D**, **G**, **J** Plotted wave image with a circular mask applied. **B**, **C**, **H**, **I** Bessel fit (red line) overlayed on sampled wave profiles plotted as displacements along the radius (**A**) (gray dots). **B** Represents the real part of the complex wave, while **C** represents the imaginary part. **E**, **F**, **K**, **L** Bessel fit of the 6% strained case. The Bessel fit accounts for shift in phase (manifesting as overlapping sinusoids that are clearest, where the gray dots are most dense). Fits for the wave number, **K**, remain stable by allowing the phase to change with each sample. Sample lines are taken from the curved outer boundary of the cylindrical cross section to the center of the converging wave. Samples are then culled to a region with the most uniformity among all experiments to avoid high variance when fitting

profile (shown as gray dots). Two significant notes are that the wave profiles are not uniform due to the non-axisymmetric geometry and from confounding factors within the sample (assumed to be prestress, anisotropy, and standing wave patterns). The first column shows the wave images, where a curl was applied to remove longitudinal waves, and a circular mask applied at the boundary to better align wave profiles. Of note, sharp changes in stress shown in Fig. 11c aligns well with the MR elastography wave image deviations on the right side of the cross section. The boundaries of the FE models have a significant impact on the wave phase as is clear in Fig. 12j on the lower right bounds.

Table 2 shows estimates of K for the MR elastography experimental data and DT informed FEA based off the closed form solution to a cylindrical boundary as described above. Relative error values are given in parentheses. At 0% total strain, the DT informed model had relative errors of 10% and 20% for the real and imaginary components. For the 6% total strain, DT informed model had 12% and 47% error.

## 4 Discussion

This paper lays out a design and application of a DT informed FE model for studying wave propagation in complex biological tissue. Figure 11 shows the complex distribution patterns of stress in a DT informed FE simulation, furthering the notion asserted by Blemker et al. of nonuniform muscle stress distribution due to fiber orientation. Qualitative analysis of the wave images compared to the stress distribution support the notion that stress effects wave propagation. Where there are deviations in stress on the cross-sectional images, there are also deviations from a concentrically propagating wave. Wave analysis showed that the DT informed model had much higher relative errors in the 6% strain cases than 0% cases. This is believed to be partly caused by the geometric boundary effects at 6% total strain, which were greater than at 0% total strain. This outcome is expected due to the derived equation's assumptions of isotropy, zero prestress, and infinite boundaries. Most current methods make the same assumptions and are expected to lead to high levels of error, as well. Currently it is not known how heterogeneous strain distributions effect wave propagation, and these differences seen in the finite-element simulations can help determine this through parametric studies.

**Table 2** Wave number ($K$) comparisons between FE approaches

| | $K_{real}$ (error) | $K_{imag}$ (error) |
|---|---|---|
| 0% | | |
| MR elastography | 833 | 242 |
| FE DT informed | 750 (0.10) | 296 (0.22) |
| 6% | | |
| MR elastography | 1061 | 369 |
| FE DT informed | 933 (0.12) | 194 (0.47) |

Further research is needed to address some limitations of the current study. Affine linear transforms could be improved upon using quaternion methods [39] for registration, as affine based registration tends to experience 'gimble lock'. Registration could also be improved upon by implementing an iterative image matching algorithm to increase reproducibility. Currently, the user must select points that match in each model, while the interface provides visual feedback, where the user then adjusts the points until the feedback is correct. Although this is sufficient for the task, matching algorithms take away user variability and provide more accurate results and have a wide usage, making it better for use beyond proof of concept [40]. Due to the scope of this paper and the issue of matching two different data types, such algorithms were not implemented, but room was given for future work. Another limitation is within the voxelwise meshing used, which will result in boundary errors in the finite-element analysis. By maintaining a smaller voxel size and tetrahedral elements, these errors are limited, but a better meshing algorithm that fills in the border should be implemented to improve robustness. Several limitations arise from wave analysis, which this paper defines in the Introduction. First, wave propagation should be interrogated from multiple polarization and propagation direction to accurately characterize material properties [7, 8, 10, 27]. The setup used in this paper preferentially creates axially polarized wave motion, which is in line with the axis of tension. Further work is currently being undertaken to develop other polarization and propagation options, where the algorithm will be leveraged in design due to its ability to induce multiple wave types in FE simulation. Waveguide (finite boundary) effects are also neglected here in the inversion algorithm, these effects may alter effect the relationship between wavelength, frequency, and material properties [12]. The Bessel fit method accounts for standing waves from the convergent cross section, but does not account for interference from other slices. This limitation means that estimates of the material properties will be inaccurate; however, iterative solutions have been used with success [41], and therefore, the previously described iterative method used as the base comparison was a way to limit the error from these limitations. Other physical limitations exist in ex vivo sample integrity. Over time, muscle samples can dry out and their material properties will change. Due to the long acquisition time of the experiments, rehydration of the muscle could only take place every 45 min. To address this, a water impermeable membrane was placed over the sample to limit evaporation. Finally, this paper focuses on the design and application of a finite-element model, not on wave theory,

only one frequency was used to compare the finite-element models to an experiment. The material properties obtained from a single frequency will be dependent on that frequency. As discussed by Papazoglou et al. [42], multiple frequencies should be measured to estimate the frequency independent material properties.

## 5 Conclusions

This work shows promising proof of concept for an algorithm that fully utilizes DT imaging to build finite-element models of complex, anisotropic structures. While the presented algorithm and methodology provide a foundation for exploration of the interplay between anisotropy, prestress and elastic moduli, and their impact on the resultant mechanical wave behavior, a number of avenues for future improvement of the overall approach are identified. Future work will leverage such FE models to interrogate the limitations listed, primarily different actuation motions, waveguide effects, and differing boundary conditions, such as radial distance, external compression, and smoother borders.

**Supplementary Information** The online version contains supplementary material available at https://doi.org/10.1007/s00366-022-01690-x.

**Acknowledgements** The authors acknowledge funding from NSF, USA Grant No. 1852691 and NIH, USA Grant No. AR071162.

**Funding** The authors acknowledge funding from NSF, USA Grant No. 1852691 and NIH, USA Grant No. AR071162.

### Declarations

**Conflict of interest** The authors have no other competing interests directly or indirectly relating to this manuscript.

## References

1. Salameh N, Larrat B, Abarca-Quinones J, Pallu S, Dorvillius M, Leclercq I, Fink M, Sinkus R, Van Beers BE (2009) Early detection of steatohepatitis in fatty rat liver by using MR elastography. Radiology 253:90–97. https://doi.org/10.1148/radiol.2523081817
2. Canu E et al (2011) Mapping the structural brain changes in Alzheimer's disease: the independent contribution of two imaging modalities. J Alzheimers Dis 26:263–274. https://doi.org/10.3233/JAD-2011-0040
3. Sack I, Jöhrens K, Würfel J, Braun J (2013) Structure-sensitive elastography: on the viscoelastic powerlaw behavior of in vivo human tissue in health and disease. Soft Matter 9:5672. https://doi.org/10.1039/c3sm50552a
4. Qin EC, Jugé L, Lambert SA, Paradis V, Sinkus R, Bilston LE (2014) In vivo anisotropic mechanical properties of dystrophic skeletal muscles measured by anisotropic MR elastographic imaging: the mdx mouse model of muscular dystrophy. Radiology 273:726–735. https://doi.org/10.1148/radiol.14132661
5. Wuerfel J et al (2010) MR-elastography reveals degradation of tissue integrity in multiple sclerosis. Neuroimage 49:2520–2525. https://doi.org/10.1016/j.neuroimage.2009.06.018
6. Guimarães CF, Gasperini L, Marques AP, Reis RL (2020) The stiffness of living tissues and its implications for tissue engineering. Nat Rev Mater 5:351–370. https://doi.org/10.1038/s41578-019-0169-1
7. Tweten DJ, Okamoto RJ, Bayly PV (2017) Requirements for accurate estimation of anisotropic material parameters by magnetic resonance elastography: a computational study: accurate estimation of anisotropic material parameters by MRE. Magn Reson Med 78:2360–2372. https://doi.org/10.1002/mrm.26600
8. Schmidt JL, Tweten DJ, Benegal AN, Walker CH, Portnoi TE, Okamoto RJ, Garbow JR, Bayly PV (2016) Magnetic resonance elastography of slow and fast shear waves illuminates differences in shear and tensile moduli in anisotropic tissue. J Biomech 49:1042–1049. https://doi.org/10.1016/j.jbiomech.2016.02.018
9. Kalra P, Raterman B, Mo X, Kolipaka A (2019) Magnetic resonance elastography of brain: comparison between anisotropic and isotropic stiffness and its correlation to age. Magn Reson Med 82:671–679. https://doi.org/10.1002/mrm.27757
10. Guertler CA, Okamoto RJ, Ireland JA, Pacia CP, Garbow JR, Chen H, Phillip PV (2020) Estimation of anisotropic material properties of soft tissue by MRI of ultrasound-induced shear waves. J Biomech Eng 142:031001. https://doi.org/10.1115/1.4046127
11. Shams M, Destrade M, Ogden RW (2011) Initial stresses in elastic solids: constitutive laws and acoustoelasticity. Wave Motion 48:552–567. https://doi.org/10.1016/j.wavemoti.2011.04.004
12. Crutison J, Sun M, Royston TJ (2022) The combined importance of finite dimensions, anisotropy, and pre-stress in acoustoelastography. J Acoust Soc Am 151:2403–2413. https://doi.org/10.1121/10.0010110
13. Strategic plan, Radiological Society of North America. https://www.rsna.org/about/reports/strategic-plan. (**Accessed Mar 02, 2022**)
14. Abramson RG et al (2015) Methods and challenges in quantitative imaging biomarker development. Acad Radiol 22:25–32. https://doi.org/10.1016/j.acra.2014.09.001
15. Chatelin S, Deck C, Willinger R (2013) An anisotropic viscous hyperelastic constitutive law for brain material finite-element modeling. J Biorheol 27:26–37. https://doi.org/10.1007/s12573-012-0055-6
16. Green MA, Geng G, Qin E, Sinkus R, Gandevia SC, Bilston LE (2013) Measuring anisotropic muscle stiffness properties using elastography. NMR Biomed 26:1387–1394. https://doi.org/10.1002/nbm.2964
17. Guidetti M, Royston TJ (2019) Anisotropic composite material phantom to improve skeletal muscle characterization using magnetic resonance elastography. J Mech Behav Biomed Mater 89:199–208. https://doi.org/10.1016/j.jmbbm.2018.09.032
18. Gennisson J-L, Grenier N, Combe C, Tanter M (2012) Supersonic shear wave elastography of in vivo pig kidney: influence of blood pressure, urinary pressure and tissue anisotropy. Ultrasound Med Biol 38:1559–1567. https://doi.org/10.1016/j.ultrasmedbio.2012.04.013
19. Wick C, Böl M, Müller F, Blickhan R, Siebert T (2018) Packing of muscles in the rabbit shank influences three-dimensional architecture of *M. soleus*. J Mech Behav Biomed Mater 83:20–27. https://doi.org/10.1016/j.jmbbm.2018.04.006
20. Kumar A, Khan NM, Anikhindi SA, Sharma P, Bansal N, Singla V, Arora A (2017) Correlation of transient elastography with hepatic venous pressure gradient in patients with cirrhotic portal hypertension: a study of 326 patients from India. World J Gastroenterol 23:687. https://doi.org/10.3748/wjg.v23.i4.687

21. Ryou M, Stylopoulos N, Baffy G (2020) Nonalcoholic fatty liver disease and portal hypertension. Explor Med 1:149–169. https://doi.org/10.37349/emed.2020.00011
22. Brinker S, Klatt D (2016) Demonstration of concurrent tensile testing and magnetic resonance elastography. J Mech Behav Biomed Mater 63:232–243. https://doi.org/10.1016/j.jmbbm.2016.06.020
23. Blemker SS, Pinsky PM, Delp SL (2005) A 3D model of muscle reveals the causes of nonuniform strains in the biceps brachii. J Biomech 38:657–665. https://doi.org/10.1016/j.jbiomech.2004.04.009
24. Sahoo D, Deck C, Willinger R (2016) Brain injury tolerance limit based on computation of axonal strain. Accid Anal Prev 92:53–70. https://doi.org/10.1016/j.aap.2016.03.013
25. Colgan NC, Gilchrist MD, Curran KM (2010) Applying DTI white matter orientations to finite element head models to examine diffuse TBI under high rotational accelerations. Prog Biophys Mol Biol 103:304–309. https://doi.org/10.1016/j.pbiomolbio.2010.09.008
26. Stadelmann MA, Maquer G, Voumard B, Grant A, Hackney DB (2018) Integrating MRI-based geometry, composition and fiber architecture in a finite element model of the human intervertebral disc. J Mech Behav Biomed Mater 85:37–42. https://doi.org/10.1016/j.jmbbm.2018.05.005
27. Manduca A, Bayly PJ, Ehman RL, Kolipaka A, Royston TJ, Sack I, Sinkus R, VanBeers BE (2020) MR elastography: principles, guidelines, and terminology. Magn Reson Med. https://doi.org/10.1002/mrm.28627
28. Bolsterlee B, Finni T, D'Souza A, Eguchi J, Clarke EC, Herbert RD (2018) Three-dimensional architecture of the whole human soleus muscle in vivo. PeerJ 6:e4610. https://doi.org/10.7717/peerj.4610
29. Yushkevich PA, Piven J, Hazlett HC, Smith RG, Ho S, Gee JC, Gerig G (2006) User-guided 3D active contour segmentation of anatomical structures: significantly improved efficiency and reliability. Neuroimage 31:1116–1128. https://doi.org/10.1016/j.neuroimage.2006.01.015
30. Clark JJ (1989) Authenticating edges produced by zero-crossing algorithms. IEEE Trans Pattern Anal Mach Intell 11:43–57. https://doi.org/10.1109/34.23112
31. Wallis SA, Georgeson MA (2009) Mach edges: local features predicted by 3rd derivative spatial filtering. Vision Res 49:1886–1893. https://doi.org/10.1016/j.visres.2009.04.026
32. Akleman E and Chen J (2005) Regular meshes. In: Proceedings of the 2005 ACM symposium on Solid and physical modeling - SPM '05, pp 213–219. https://doi.org/10.1145/1060244.1060268
33. Grant JA (1970) Chebyshev polynomials in numerical analysis. Math Gaz 54:96–97. https://doi.org/10.2307/3613223
34. Yeh F-C, Verstynen TD, Wang Y, Fernández-Miranda JC, Tseng W-YI (2013) Deterministic diffusion fiber tracking improved by quantitative anisotropy. PLoS One 8:e80713. https://doi.org/10.1371/journal.pone.0080713
35. Hormann K, Agathos A (2001) The point in polygon problem for arbitrary polygons. Comput Geom 20:131–144. https://doi.org/10.1016/S0925-7721(01)00012-8
36. Lorensen WE and Cline HE (1987) Marching cubes: a high resolution 3D surface construction algorithm. In: SIGGRAPH '87: Proceedings of the 14th annual conference on Computer graphics and interactive techniques, 7. https://doi.org/10.1145/37401.37422
37. Yasar TK, Royston TJ, Magin RL (2013) Wideband MR elastography for viscoelasticity model identification. Magn Reson Med 70:479–489. https://doi.org/10.1002/mrm.24495
38. Klatt D, Yasar TK, Royston TJ, Magin RL (2013) Sample interval modulation for the simultaneous acquisition of displacement vector data in magnetic resonance elastography: theory and application. Phys Med Biol 58:8663–8675. https://doi.org/10.1088/0031-9155/58/24/8663
39. Walimbe VS, Zagrodsky V, Raja S, Bybel B, Kanvinde M, Shekhar R (2004) Elastic registration of 3D whole body CT and PET images by quaternion-based interpolation of multiple piecewise linear rigid-body registrations. Med Imaging 5370:119. https://doi.org/10.1117/12.535501
40. Hill DLG, Batchelor PG, Holden M, Hawkes DJ (2018) Medical image registration. Phys Med Biol. https://doi.org/10.1088/0031-9155/46/3/201
41. Fovargue D, Kozerke S, Sinkus R, Nordsletten D (2018) Robust MR elastography stiffness quantification using a localized divergence free finite element reconstruction. Med Image Anal 44:126–142. https://doi.org/10.1016/j.media.2017.12.005
42. Papazoglou S, Hirsch S, Braun J, Sack I (2012) Multifrequency inversion in magnetic resonance elastography. Phys Med Biol 57:2329–2346. https://doi.org/10.1088/0031-9155/57/8/2329